ADVANCED ENERGY MATERIALS
www.advenergymat.de

Quantifying Heterogeneous Degradation Pathways and Deformation Fields in Solid-State Batteries

Ji Hu, Robert Scott Young, Bratislav Lukic, Ludovic Broche, Rhodri Jervis, Paul R. Shearing, Marco Di Michiel, Philip J. Withers, Alexander Rettie, and Partha P. Paul**

Solid-state batteries are compelling candidates for next-generation energy storage devices, promising both high energy density and improved safety, by utilizing metallic Li as the negative electrode. However, they suffer from poor cyclability and rate capability, which limits their wide application. Degradation in these devices occurs through complex mechanical, chemical and electrochemical pathways, all of which produce heterogeneous deformation fields. Therefore, isolating solid-state degradation mechanisms, and explicitly linking them to the associated deformation fields requires a multimodal characterization strategy. Here, a novel 3-D, in situ methodology for linking degradation to deformation in solid-state cells is presented. X-ray imaging is used to measure the morphological degradation, and combined with X-ray diffraction to quantify (electro)chemical aspects. Finally, the heterogeneous stress fields from these various pathways are mapped in situ. This heterogeneity is shown *globally*, from the interface to the bulk electrolyte, as well as *locally*, around features such as cracks and voids. Through these analyses, it is possible to delineate the effects of solid electrolyte processing, cell assembly, and cycling on the end-of-life state of the cell. Moreover, the importance of stress mitigation in these cells is highlighted, with mean stresses around the interface and some cracks comfortably exceeding the elastic limit of Li.

1. Introduction

As we transition toward rechargeable technologies powering the transportation and 3C sectors (computer, communication and consumer electronic products), there is an immediate need for improved energy storage devices. Solid-state batteries (SSBs) have been explored as a promising route to enhanced energy density and safety compared with conventional Li-ion batteries (LIBs).[1,2] The use of a solid electrolyte (SE) could enable lithium metal as the negative electrode material, which has advantages over intercalation electrodes such as graphite. Li has the lowest reduction potential of any known element (3.04 V vs the standard hydrogen electrode) and a high theoretical specific capacity (3860 mAh g^{-1}).[3] As LIBs use flammable liquid electrolytes, replacement with a SE also improves safety by mitigating leakage and thermal run-away events.[4] Despite these advantages, large-format SSBs have not achieved wide commercial deployment, primarily due to challenges at numerous solid–solid interfaces and during moderate to high rate operation, which typically results in rapid cell failure.[5,6] This can lead to cracks forming in this region, and growing through the bulk of the SE. Subsequently, these can become filled with metallic Li, leading to electronic shorting of the cell.[7] Thus, a key goal in the field is to understand, and mitigate degradation at the Li-SE interface.

J. Hu, R. S. Young, R. Jervis, P. R. Shearing, A. Rettie
Department of Chemical Engineering
University College London
London WC1E 6BT, UK
E-mail: a.rettie@ucl.ac.uk
J. Hu, R. S. Young, R. Jervis, P. R. Shearing, A. Rettie
The Faraday Institution, Quad One
Harwell Science and Innovation Campus
Didcot OX11 0RA, UK
B. Lukic, L. Broche, M. Di Michiel, P. P. Paul
ESRF - The European Synchrotron
71 Avenue des Martyrs, Grenoble 38000, France
E-mail: ParthaPaul2018@u.northwestern.edu
B. Lukic, P. J. Withers, P. P. Paul
Henry Royce Institute
Department of Materials
The University of Manchester
Manchester M13 9PL, UK
P. R. Shearing
Zero Institute
University of Oxford
Oxford OX2 0ES, UK
The ORCID identification number(s) for the author(s) of this article can be found under https://doi.org/10.1002/aenm.202404231

© 2024 The Author(s). Advanced Energy Materials published by Wiley-VCH GmbH. This is an open access article under the terms of the Creative Commons Attribution License, which permits use, distribution and reproduction in any medium, provided the original work is properly cited.

DOI: 10.1002/aenm.202404231

In this regard, we define *"degradation"* as the various mechanisms by which a system deteriorates over time. For example, degradation at the interface of an SE occurs through a multitude of mechanical, chemical and electrochemical pathways,[8] and are spatially inhomogeneous. Next, we define *"deformation"* as a measurable change in the system behavior, due to a degradation process, e.g., strain. Thus, *multimodal* characterization strategies that can identify these various pathways and their interactions are required, necessitating 3D spatially resolved datasets.[9] In the context of an SSB, the "electro-chemo-mechanical" degradation pathways that influence cell behavior can be measured *locally* in terms of the strain field, or *globally* in terms of the capacity retention during cycling. In the presence of multiple degradation pathways, it is important to establish links between individual degradation mechanisms, and the resultant deformation (strain/stress field). Such relationships can improve our understanding of SSB degradation and help identify strategies to enable long-lifetime solid-state devices.

Among inorganic SEs, sulfide-based electrolytes have demonstrated ionic conductivity up to 2.5×10^{-2} S cm^{-1}[10] – comparable to that of liquid electrolytes.[11] In this material class, lithium thiophosphate chloride (Li_6PS_5Cl) with the argyrodite crystal structure is commonly used as a model system because it possesses high ionic conductivity (>10^{-3} S cm^{-1}), forms a relatively stable passivation layer in contact with Li metal and can be acquired from commercial sources. However, there are several disadvantages as well: i) the passivation layer contains Li_2S and Li_3P[12,13] which can increase the cell impedance, ii) despite its malleability compared to oxide-based SEs for example, it is brittle and can undergo extensive cracking,[14] and iii) its high sensitivity to air and moisture.[15] With all of these points in mind, this work will focus on understanding the degradation in Li_6PS_5Cl-based cells.

Li-based systems are challenging to characterize, due to the high reactivity and low density of Li.[16] Recently, there has been a marked push toward *operando* or in situ characterization of interfacial degradation, primarily using 2D or 3D imaging-based methods,[17] such as X-ray microcomputed tomography (μ-CT),[18,19] optical microscopy[20,21] and electron microscopy.[22,23] Sun et al.[24] used μ-CT, along with complimentary experimental and modeling to link interfacial degradation in SSBs via mechanical, and electrochemical pathways. Tippens et al.[19] showed that an interphase develops between a sulfide-based SE and Li, and grows over cycling, resulting in interfacial stresses that cause nucleation and propagation of filaments. Narayanan et al.[25] investigated the chemical and electrochemical degradation at interface between Li metal and Li_6PS_5Cl, and connected it to the critical current density, while Zheng et al.[26] showed an uneven Li-ion flux to be responsible for cathode/anode side degradation. Porz et al.[27] used a combination of *operando* methods, to study the close entanglement between pre-existing defect structures in the SE, the applied current density, opening of cracks in the SE, and the propensity for Li to fill the cracks and short the SSB, while Duan et al.[28] similarly calculated stress fields from heterogeneous plating/stripping to be adequate for microscopic crack opening in the SE.

While these studies have provided novel information on SSB degradation, two primary gaps are largely unexplored so far. First, a way to isolate, and quantify the various degradation pathways is essential. Second, the complex interplay between SSB degradation and stress fields has been a focus of a few recent works.[29–32] However, explicit links between various degradation mechanisms (mechanical/(electro)chemical) and the deformation fields created are currently lacking. For this, a combination of multimodal, non-destructive techniques are needed. Such multidimensional datasets would be invaluable for modeling studies to robustly interrogate universal underlying causes of failure in SSBs.

Therefore, to better understand the relationship between degradation and the resultant deformation fields in SSBs, we combine complementary 3D in situ X-ray techniques. Conducting such experiments at a synchrotron source allows one to obtain 3D datasets with microscale spatial resolutions and scanning time that are orders of magnitude faster than in standard laboratory set-ups. First, μ-CT imaging is used to analyze the morphological degradation in the SE (measured as voids, pores and cracks; henceforth referred to as cracks for simplicity). Then, 3D resolved X-ray diffraction computed tomography (XRD-CT) is applied to quantify various phases in the cell, providing insights into chemical and electrochemical reaction products. Finally, XRD-CT is used to analyze the volumetric stress, and relate degradation to deformation *globally*, in the context of the whole device, and *locally*, around degradation hotspots (such as cracks and secondary phases). This approach is used first on an as-assembled cell, and then on a cell that has been cycled to failure. The objective of such an approach is to isolate the effects of SE processing and cell assembly, from electrochemical cycling with a high degree of spatial resolution and chemical sensitivity. While μ-CT is more extensively used, spatially resolved XRD-CT based analyses have only recently provided insights into the spatial heterogeneity of degradation in energy storage devices, specially electrode materials.[33–37] However, XRD-CT has not yet been applied to SSBs to the best of our knowledge. Additionally, the combination of μ-CT and XRD-CT to correlate degradation mechanisms and deformation mechanisms is largely unexplored in general. Correlating deformation with degradation shows that most cracks formed in the SE over the various steps of the cell life do not have an elevated strain around them, likely not contributing to the cell failure. The diversity of such "electro-chemo-mechanical" degradation mechanisms and resulting from the various steps in the life cycle of a cell from SE processing and cell assembly, to electrochemical cycling, as well as the heterogeneity of deformation fields in SSBs make them ideal candidates for such a combined 3D in situ approach.

2. Results and Discussion

Two cylindrical, symmetric cells (Li|Li_6PS_5Cl|Li) were used for this study. One cell was scanned in the pristine, as-assembled state (referred to as the *pristine cell*), while the second cell was cycled to failure (referred to as the *shorted cell*). The *shorted cell* was cycled without additional stack pressure, at room temperature. A current density of 0.3 mA cm^{-2} was applied during alternating plating and stripping periods before the cell electrically shorted after ≈12 h.

© 2024 The Author(s). Advanced Energy Materials published by Wiley-VCH GmbH

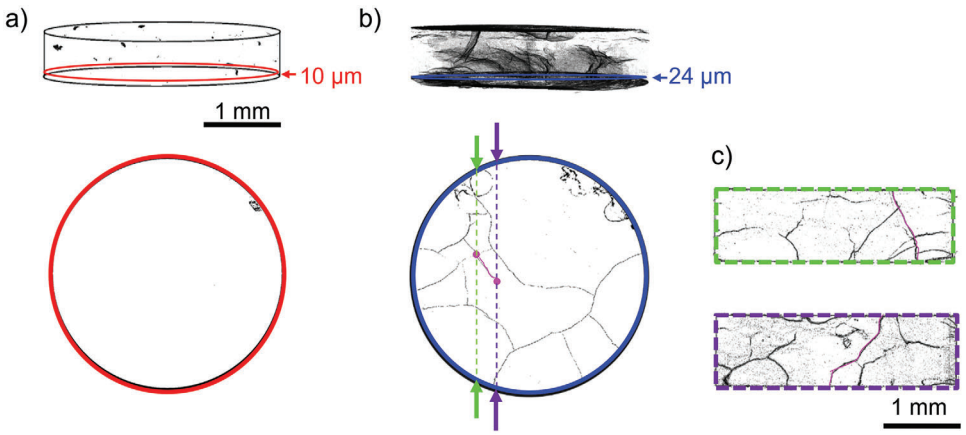


Figure 1. Morphological degradation in the SE, revealed by µ-CT. a): *pristine cell*. The top panel shows 3D rendering of the SE pellet, while the bottom panel shows a cross-sectional slice close to the Li | SE interface highlighted by the red slice. b,c): *shorted cell*. (b) shows the 3D rendering and a cross-sectional slice that is close to the interface. The difference in morphological degradation between the *pristine cell* and *shorted cell* are clearly visible. (c) shows a perpendicular view of two slices in (b), highlighted by the colored arrows and dotted lines in (b). The cracks extending through the thickness of the pellet (termed 'terminal' cracks) are highlighted by magenta in (b) and (c).

2.1. Mapping Morphological Degradation by µ-CT

Figure 1 shows the morphology of the *pristine cell*, compared to a cell that was cycled to failure (the *shorted cell*). The volume and cross-sectional areas have been cropped to display just the SE pellet. The *pristine cell* appears largely uniform, with the exception of a few solitary voids (Figure 1(a)). In contrast, the *shorted cell* displays a large number of cracks, emanating from either the top or bottom interfaces as shown in Figure 1b. By analyzing a cross-section close (45 µm) to the top interface with Li, a large number of these cracks span the diameter of the cell (Figure 1b). In Figure 1c, cracks that traverse the entire thickness of the SE are evident. Short circuiting of the cell likely occurred through one or more of these pathways. As the SE microstructure was highly reproducible between pristine cells (see data for a second pristine cell in Figure S4, Supporting Information), any cracking can be considered to be a result of electrochemical cycling. As the exact physical path for electrical shorting of the cell was unclear, we treat all cracks extending the height of the SE as equally likely sites for this failure event, and term them "terminal" cracks.

In summary, we observed extensive morphological degradation of the SE and a larger concentration of defect structures close to the interfaces of Li_6PS_5Cl with Li metal in the *shorted cell* compared to the *pristine cell*. These results are consistent with earlier studies that observed a larger density of cracks around the interfaces in SSBs using µ-CT.[18,30,32] We note that the cracks shown here do not represent all such features across length scales present in the SE; only those that are above ≈5 µm could be reliably segmented due to the voxel size of 0.7 µm.

2.2. Phase Analysis by XRD-CT

X-ray diffraction computed tomography (XRD-CT) furnishes 3D spatially resolved diffractograms of a volume, which allows for phase quantification, as well as strain analyses. **Figure 2** shows a representative µ-CT slice of the *shorted cell*, and the corresponding XRD-CT phase. Several cracks are immediately visible throughout the cross-section in Figure 2 (top left), the largest of which is highlighted. This crack was clearly visible in the phase map of Li_6PS_5Cl in Figure 2, as well as a region with a relatively low amount of Li_6PS_5Cl (highlighted by the purple ellipse). It was evident by comparison with the CT slice this region had a density similar to Li_6PS_5Cl and was therefore not a void. Rather, XRD-CT showed this region to be rich in Li_2CO_3 and LiCl, with a noticeable level of Li_2S. Li_2S and LiCl are commonly used as precursors for synthesizing Li_6PS_5Cl, pointing toward pockets of unreacted precursor material in the SE, as observed in similar material by Randrema et al.[38] Therefore, this low Li_6PS_5Cl volume fraction zone (≈80%) is likely from unreacted precursor materials, as highlighted by the purple circle in Figure 2. These are also extremely air sensitive, and can react with small amounts of CO_2 to form Li_2CO_3. This phenomenon is discussed in further detail in the subsequent sections. Other residual chemical phases from the heat treatment procedure are evident in Figure 2, such as carbon, and Li_2C_2 when carbon reacts with Li. Such heat treatment using carbon-coated fused-silica ampules is a common method for synthesizing such SEs.[30,32] This is typically done to reduce the exposure of the SE to moisture and air. However, Zhou et al. hypothesized that small amounts of remnant moisture from the quartz tubes can also react with the SE,[39] thus creating more impurities. Additionally, there is the unintended consequence of formation of Li_2C_2 in the SE, which has not been observed previously. It should be emphasized that many of these impurity phases produce very weak peaks compared to Li_6PS_5Cl, therefore identifying and quantifying such phases is extremely challenging without access to very high-quality (low noise) diffractograms as obtained at synchrotron light sources. Due to their similar densities, such phases cannot be observed without chemical mapping, emphasizing the utility of such a multimodal characterization strategy. Importantly, this study highlights avenues for improving the SE processing and cell assembly steps from the established standards practiced currently, in order to prepare SEs with a better purity.

While some crack structures in the µ-CT slice are correlated with the presence of Li_2CO_3, the large crack marked with the

© 2024 The Author(s). Advanced Energy Materials published by Wiley-VCH GmbH

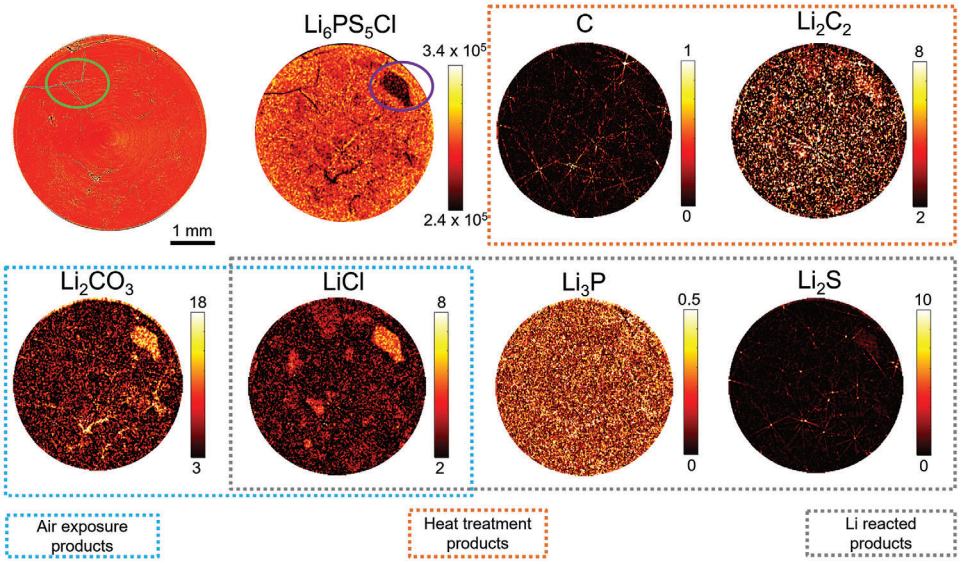


Figure 2. μ-CT image (top left) and the corresponding phase maps for a cross-sectional slice at a depth of 120 μm from the Li | Li_6PS_5Cl interface in the *shorted cell*. These phases span heat treatment, air exposure, as well as other Li products (Li_6PS_5Cl reduced by Li metal from cell cycling, or synthesis precursors), as indicated by the differently colored boxes. The colorbar for Li_6PS_5Cl indicates the integrated intensity of the (111) peak in arbitrary units, which is proportional to the volume of the material. The colorbars for all other phases all denote the volume % of that phase.

green ellipse was not. One possible explanation for this observation is that this is a crack formed during cycling of the cell. Cracks that exist prior to or are produced early during cycling have the opportunity to react with any remnant air to form Li_2CO_3. On the other hand, a crack formed late in cycling, which is in turn filled with Li would not. The Li_3P and Li_2S observed in Figure 2 are the electrochemical degradation products expected from Li_6PS_5Cl in contact with Li.[13] The volume percentage of Li_3P was the smallest among all phases recognized (at less than 0.5 volume %) and so will not be discussed in detail further.

2.3. in situ Measurement of Strains/Stresses

XRD-CT also permits the calculation of 3D elastic strain. By tracking the change in unit cell volume of any phase identified in XRD-CT, the strain across the cross-section and through the depth of the SE was measured. Here, we used the change in the unit cell volume of Li_6PS_5Cl at each voxel, compared to the mean unit cell volume of Li_6PS_5Cl in the bulk of the SE to calculate the volumetric strain as:

$$\mathcal{E} = \frac{a^3_{Li_6PS_5Cl} - a^3_{mean}}{a^3_{mean}} \quad (1)$$

where, a represents the lattice parameter of Li_6PS_5Cl at every voxel obtained from XRD refinement, and a_{mean} stands for the reference lattice parameter. This volumetric strain was then converted into the volumetric stress using the bulk modulus (K) of Li_6PS_5Cl.

Here, we note a few points pertinent to these calculations:

1) This approach focuses on the longer range (sometimes called engineering) strains between regions that gives rise to peak shifts, rather than the very short range strains that give rise to diffraction peak broadening.
2) The elastic stress was measured using the Li_6PS_5Cl phase. While a similar calculation can be carried out with respect to any phase, Li_6PS_5Cl was chosen since this is the dominant phase and produces the most intense and separable XRD peaks.
3) The mean unit cell values were calculated for every cross-sectional area like the one shown in Figure 2. This unit cell volume was calculated as a weighted mean, to account for the different amounts of Li_6PS_5Cl in each location of a cross-sectional area.
4) In the *shorted cell*, the bulk SE was considered to be in an overall stress-free state. To calculate the reference unit cell volume of Li_6PS_5Cl we used regions that were more than 15 μm away from the interface, as the mean values remain constant (<0.1% change) at distances greater than 15 μm and so constitute the bulk.
5) This methodology calculates the equivalent isotropic volumetric strain. i.e. a weighted average value of the elastic strain along the different directions. While the stress generated in the cell is not isotropic in reality, this calculation yields an isotropic approximation of the 3D stress generated. Thus, the strain (stress) referred to henceforth in this work refers to this volumetric strain (stress).
6) A positive value indicates a tensile state of stress, while a negative value connotes a compressive stress.

Finally, we note that the high energy of X-rays used results in >95% transmission through the cells, thus the penetration depth of X-rays through the sample does not have an effect on such analyses.

© 2024 The Author(s). Advanced Energy Materials published by Wiley-VCH GmbH

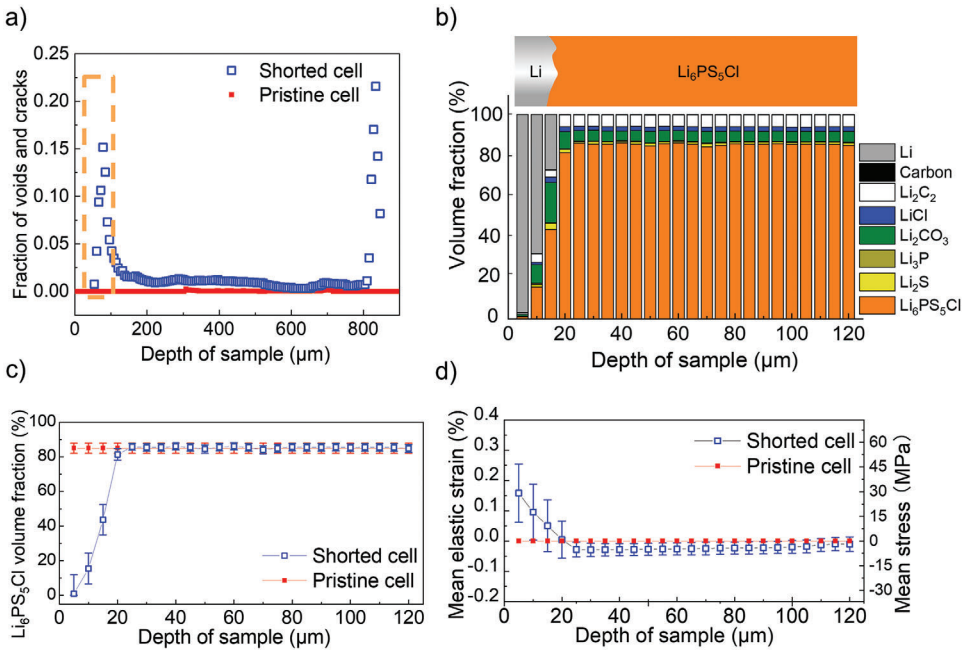


Figure 3. Global imaging, phase and strain/stress analyses. a) Crack fraction as a function of the SE depth in the *shorted* and *pristine cells*. Increased crack fractions at the interfaces are clearly visible. b) Phase fractions of all phases identified in XRD-CT as a function of distance from the Li-Li_6PS_5Cl interface in the *shorted cell* (highlighted by the cyan box in (a). c) Li_6PS_5Cl phase fractions for both cells as a function of distance from the Li-Li_6PS_5Cl interface. d) Resultant elastic strain (left) and stress (right) in the Li_6PS_5Cl SE due to the degradation shown in (a–c), showing a higher mean stress, and stress variation closer to the interface.

2.4. Global Heterogeneity in Deformation

Figures 1 and 2 have shown the various modes of degradation that can be measured in the cell, qualitatively. This section aims to first quantify the degradation mechanisms discussed earlier, and then measure the resultant stress in the cell due to the degradation mechanisms. **Figure 3**a quantifies the fraction of cracks present at each height of the SE, in the *pristine cell* and the *shorted cell*. It can be seen that:

1) the *pristine cell* has a significantly lower number of cracks compared to the *shorted cell*, both at the interfaces with Li metal, and in the bulk of the SE.
2) the *shorted cell* has a significantly larger fraction of cracks close to each interface (>20%), compared to the SE bulk (≈1–2%).

Figure 3b shows the phase fractions of the SE, and various degradation products as a function of the distance from the Li-SE interface. These data were obtained by averaging the phase fractions for every phase over the entire cross-section (like those shown in Figure 2) at each depth of XRD-CT measurement (indicated by the dotted cyan box in Figure 3a). Close to the interface, the amount of Li was obtained by segmentation of the μ-CT slices corresponding to the appropriate XRD-CT slice. This was done because quantification of Li using the XRD signal was challenging (detailed methodology is provided in the Section S3, Supporting Information). Immediately from Figure 3b, a decrease in the volume fraction of Li_6PS_5Cl near the interface (20 μm) was evident, coinciding with an increase in many minor phase fractions relative to Li_6PS_5Cl in this region. In particular, a marked increase in the air exposure product Li_2CO_3 was observed. Air exposure and/or decomposition products, LiCl and Li_2S, also showed a noticeable increase close to the interface, though not as pronounced as Li_2CO_3. The sum of remnant species from heat treatment (Li_2C_2 and graphite) was comparable with the bulk.

These observations can be rationalized based on the following arguments. The reaction of the SE with Li metal is greatest at the interface, thereby forming various characteristic reaction products. Additionally, air leakage occurs over time and areas with a higher concentration of cracks, such as the outer surface of the pellet or the Li-SE interface, have a higher potential for reaction with air to form Li_2CO_3. Finally, the pre-existence of a larger concentration of defect structures (voids and secondary phases) at the interface produces heterogeneous stresses that can lead to nonuniform plating/stripping. This in turn causes more electrochemical redox products to form at the interface as the cell is cycled. Such behavior has been seen previously in both modeling[40] and experimental[31] studies, where pre-existing defect structures create electrochemical or mechanical stress fields around them, thus exacerbating the degradation around them during further cycling.

From the *pristine cell* depth profile shown in Figure 3c, a constant Li_6PS_5Cl volume fraction of ≈85% was found, with the remainder constituting various degradation products. The ≈15% of secondary phases present before cycling highlights the importance of SE production, processing and cell assembly steps on the composition of these devices. The behavior of the Li_6PS_5Cl volume fraction in the *shorted cell* is consistent with Figure 3b, but also showed a large increase in the variability of this value as the interface was approached, which is calculated as one standard

© 2024 The Author(s). Advanced Energy Materials published by Wiley-VCH GmbH

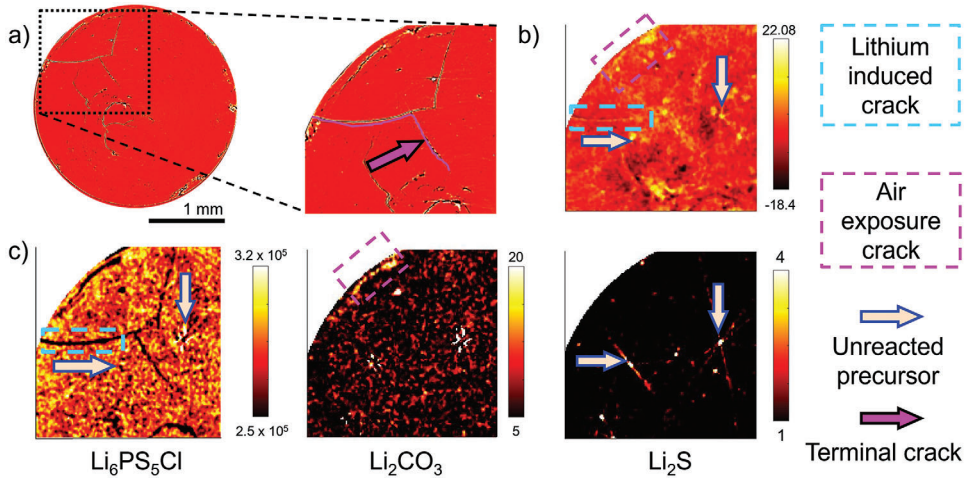


Figure 4. Local mapping of degradation mechanisms and deformation in an area close (20 µm) to the interface. a) Crack distribution using µ-CT, with a zoomed-in area. b) Stress (MPa) of the Li_6PS_5Cl phase in the region corresponding to the zoomed-in area in (a). c) Phase fractions (in %) for the region in (b) from XRD-CT analyses. Features of interest are highlighted by different markers, based on the likely degradation mechanism. In (c), the colorbar for Li_6PS_5Cl indicates the integrated intensity of the (111) peak, which is proportional to the volume of the material, while the colorbars for Li_2CO_3 and Li_2S represent the phase fraction.

deviation of all voxels belonging to a particular distance from the interface. This result can be explained with the aid of the imaging analyses in Figure 3a, where a larger number of void structures such as cracks result in a larger variability in the amount of Li_6PS_5Cl.

Thus far, we have seen that the Li–Li_6PS_5Cl interface exhibited substantially higher morphological, chemical, and electrochemical degradation compared to the bulk SE. The resultant stress/strain is plotted as a function of distance in Figure 3d, obtained as described in Section 2.3. The *pristine cell* exhibited near-zero stress at all depths, consistent with negligible cracks and limited chemical reactions in this state. On the other hand, the mean value of stress was small and negative until the interface was reached in the *shorted cell*. Here, the mean and variance increased dramatically, with the former becoming positive. The positive value of stress indicates that this is the interface where stripping was the last step prior to cell failure. The larger variation in stress points toward a more heterogeneous stress field closer to the interface, implying either a larger concentration of defect sites with heterogeneous fields around them, or stronger heterogeneous fields around individual sites of of degradation, or both. The mean value of stress closest to 0 µm in Figure 3d is instructive. Converting the volumetric strain into the equivalent stress using the bulk modulus of Li_6PS_5Cl (18.4 GPa[41]), this stress (≈30 MPa) is more than an order of magnitude larger than the yield stress for macroscopic Li (≈1 MPa[42]); the peak stresses are even higher. The range of strain at a depth of 15 µm, adjacent to the Li electrode, is between –0.04% and ≈ +0.15%, which is within same range reported by Ning et al.[32] Thus, at the interface, the degradation results in a mechanical stress field sufficient to push metallic Li into any cracks that have formed at that interface. Around deformation sites, this value is even higher, as evidenced by the large variation in the stress. We note here that the elastic limit of Li is size dependent,[43] as well as temperature and stress-rate dependent,[44] with values over a couple of orders of magnitude being reported.

2.5. Local Heterogeneity of Degradation Mechanisms and Deformation

To build on the picture of increased degradation and resultant deformation around the interface in the previous section, the different degradation types, as well as the resultant stress relatively close to, and far from the interface were analyzed for the *shorted cell*. Areas were chosen such that they were under a global, macroscopic stress of ≈0 MPa, in order to examine local stress (strain) in these regions.

Figure 4 reveals the spatially-resolved degradation and deformation in a cross-sectional slice close (20 µm) to the Li-Li_6PS_5Cl interface. A high concentration of cracks in the top left quadrant of the SE pellet is indicated in Figure 4a. Several corresponding regions of high tensile stress were observed (Figure 4b), which warrant comparison. The largest crack, clearly seen in Figure 4a,c, is considered first. A stress gradient across the horizontal arm of the crack (cyan boxes in Figure 4b,c) from tensile to compressive is observed, corresponding to a stress (strain) gradient of >18 MPa (0.1%). This region clearly shows a lower volume of SE, consistent with a crack in the SE being present. This crack changes direction at multiple points, and exhibits several branches. One of these branches is a terminal crack (indicated by the pink arrow in Figure 4a, i.e., it extends through the thickness of the SE. This feature is correlated with high tensile stress in Figure 4b. We reiterate here that the calculated local stress (strain) is an isotropic equivalent of the actual local stress (strain).

Next, an edge region of high tensile stress is discussed (see pink dashed box in Figure 4b). Numerous cracks can be observed via µ-CT in Figure 4a. The same region shows a clear spike (>15%) in the amount of Li_2CO_3 (Figure 4c). Since Li_2CO_3 can only be formed by the presence of CO_2 reacting with Li_6PS_5Cl, this is referred to as an *air exposure crack*. Thus, despite being sealed in an Ar-filled glovebox, this cell shows regions affected by air exposure, which create regions with SE degradation products, and a high concentration of mechanical stress. We note

© 2024 The Author(s). Advanced Energy Materials published by Wiley-VCH GmbH

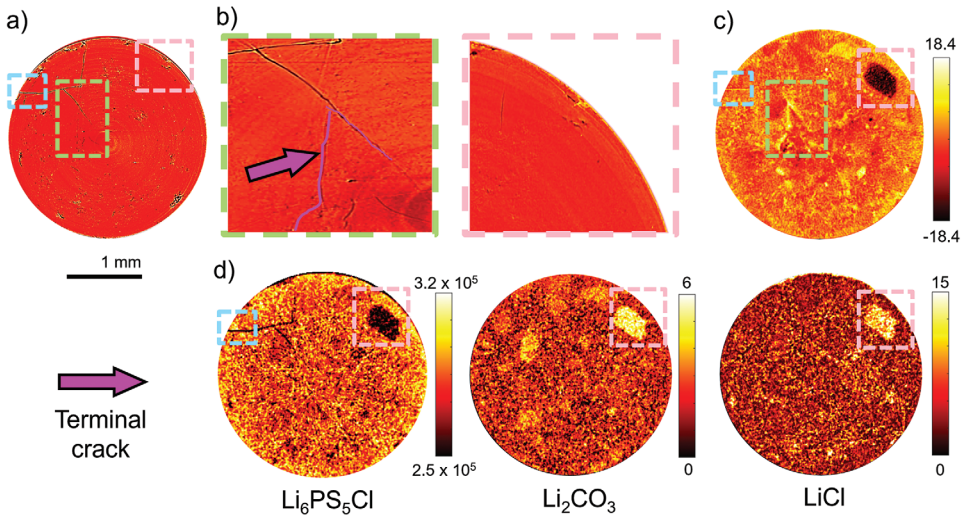


Figure 5. Local mapping degradation mechanisms and deformation in area far (80 µm) from the interface. a–c) cracks revealed by µ-CT. Two regions of interest in (a) are shown in the µ-CT images in (b), showing various crack structures. (c) shows the elastic stress (MPa) from the Li_6PS_5Cl phase, with a highlighted box showing the same region as Figure 4. d) Phase fractions (in %) for the whole cross-section in (a).The colorbar in (d) for Li_6PS_5Cl indicates the integrated intensity of the (111) peak; proportional to the volume of the material, while the other two phases show the phase fraction.

that Li_2CO_3 signatures were not found in the cracks in the cyan box in Figure 4c, despite this feature also extending to the outer edge of the SE, indicating a different underlying cause. Additionally, other hotspots of tensile stress were identified (arrows in Figure 4b). These regions can be rationalized by the XRD-CT analyses (Figure 4c), where spikes in the amount of Li_2S were seen. As these are micron-scale, isolated pockets of Li_2S, they are assigned to unreacted precursor material as opposed to decomposition of the SE against the Li metal electrode. Finally, there is one additional region of high tensile stress, toward the bottom center of the stress map in Figure 4b, which is in close vicinity to the large network of cracks in Figure 4a.

Next, we analyze a second cross-section from a region significantly further away (80 µm) from the Li-Li_6PS_5Cl interface in **Figure 5**. Figure 5a shows an µ-CT cross-sectional slice. Compared to Figure 4a, there are relatively fewer cracks here, which is consistent with greater morphological degradation occurring closer to the interface, as seen previously (Figures 1 and 3). For reference, the cyan box in Figure 5a corresponds to the same crack in Figure 4. Two new areas of interest are shown in Figure 5b; the first shows a crack network close to the center of the slice (green box), with several branches while the second shows a network of voids near the edge of the SE (pink box). Figure 5c shows the elastic stress (in MPa) obtained from the XRD-CT analysis of the SE. The cyan box shows the same tensile-to-compressive stress gradient across the horizontal arm seen for the same crack closer to the interface in Figure 4c. On the other hand, the green box corresponding to the region in Figure 5b shows a clear area of structured tensile stress. The pink arrow highlighting this box is the "terminal crack," also shown in Figure 4. This terminal crack, which is the most likely location at which the cell short-circuited via Li filaments, shows a clear spike in tensile stress (≈20 MPa): far exceeding the yield stress of metallic Li. It is important to note that not all of the deflected cracks in Figure 5b show as high tensile stress in Figure 5d as the terminal crack.

Finally, we consider the large region of relative compressive stress (pink box in Figure 5d). Interestingly, this region does not correspond to any voids or cracks, suggesting that this region has a similar density to the Li_6PS_5Cl SE. A closer examination of the phase maps in Figure 5d show a relatively lower amount of Li_6PS_5Cl, but a higher amount of Li_2CO_3 and LiCl. This suggests a volume of poorly mixed precursor material that reacted with air. A closer examination of this region in Figure 5c shows a network of voids lying between the outer edge of the SE pellet and this volume. Therefore, we hypothesize that this void network provided a pathway for ambient air, likely due to imperfect sealing of the Swagelok cell, to reach the pocket of unmixed precursor materials, which then produced Li_2CO_3 in that region, and caused a stress hotspot in the region.

2.6. Discussion

In the preceding sections, we have seen numerous causes for high deformation (stress), from cycling, to air exposure (cell assembly), and processing of the SE. Cylindrical Swagelok-style cells are commonly used in the study of air-sensitive materials and electrochemical devices. When prepared in an inert-gas glovebox, it has been considered a safe assumption to attribute all subsequent cell degradation to cycling. By deconvoluting the physical defects and resultant stress fields using XRD-CT, the importance of both the SE processing and cell assembly in influencing deformation have been shown. This is surely dependent on the type of SE used, and its reactivity. Sulfide-based electrolytes, which are typically attractive for their high ionic conductivity are also notoriously reactive with trace amounts of moisture/air.[15] Therefore, this study reinforces that in lab-assembled cylindrical cells with such electrolytes, the material processing and cell assembly can also influence the cell behavior significantly. Therefore, before we progress toward multimodal *operando* 4D studies from the in situ 3D investigations presented here, or large-format

© 2024 The Author(s). Advanced Energy Materials published by Wiley-VCH GmbH

commercial cells, the challenges associated with assembly, air tightness, and materials processing must be addressed first. In practice, there will always be some level of air exposure as large format solid-state batteries will be fabricated in dry rooms with reduced (but not zero) moisture content. Exposed surfaces will be most affected and become interfaces where degradation is concentrated. Our results point to decomposition by-products (for example, Li_2CO_3) that will be pertinent to real-world situations such as slow leakage and catastrophic failure events. Therefore, although the effects of air exposure will be lessened in commercial solid-state batteries, they are still relevant; especially to the devices currently being made in research labs and at smaller scales (e.g., using Swagelok cells).

Another intriguing aspect in the cell design is the influence of SE microstructure and the global stress state of the cell on the nucleation and propagation of cracks through the SE respectively. It was recently shown[45] that the SE microstructure (such as grain size, that can be controlled by ball milling of the SE) plays an important role in inducing interfacial defects that lead to cell failure. Lee et al.[46] studied the effect of global stack pressure on the formation of Li dendrites in symmetric $Li|Li_6PS_5Cl|Li$ cells, where a higher stack pressure appeared to cause faster failure of the cell. Fincher et al.[47] also showed how the lateral mechanical stress state interacts with crack deflection in brittle SEs, where lateral crack deflection decreases the brittle nature of fracture in the SEs, while also creating a more tortuous crack path through the SE. This has important implications for Li filling such cracks, as Hao et al.[18] observed Li deposits tending to fill regions of cracks with a relatively lower curvature. Taken altogether, the onus is to design a cell for in situ studies that can minimize negative outcomes of cell preparation/assembly, while optimizing the cell structure/SE microstructure in a way to prolong cycling life. In addition to the implications for cell construction and cell life, the measurement of 3D stress fields and phase maps is an invaluable tool for the modeling community. For a deeper understanding of SSB degradation, as well as designing rational strategies to stabilize them, there is a pressing need for a combination of experimental and modeling efforts, as was summarized by Xiao et al.[48] Currently, the models propose various deformation mechanisms in SSBs, especially at the interface.[49] In general, these are compared to singular experimental datasets, such as those from μ-CT. By matching the morphological degradation to these, the resultant deformation (stress fields) are predicted. Hence, such modeling efforts tend to match specific studies well, but have limited applicability beyond them. However, this approach presents a unique challenge for electrochemical systems, where numerous degradation pathways exist. Imaging techniques often require lesser time and can often provide excellent spatial resolution on mechanical degradation, lending themselves to in situ and operando studies. However, secondary reaction products arising from (electro) chemical reactions usually have similar densities to the primary material, thus distinguishing them through imaging can be challenging. Additionally, strain estimation done with just imaging using digital volume correlation is only sensitive to macroscopic volumetric changes, thus characterizing strains that have a (electro)chemical origin require an additional method that is sensitive to such chemical information, such as the XRD-CT used here. Thus, utilizing 3D, in situ, and most importantly multimodal analyses such as the ones presented here will be an invaluable tool in this regard. Not only are the degradation modes identified, the resultant deformation fields are also quantified, providing a clear direction for which degradation modes to prioritize addressing.

In this discussion of stress concentrations through the SE volume, we note that not all deformation features, such as cracks, have an elevated stress field around them in the *shorted cell*. This distinction between deformation features is important, especially in brittle SEs such as argyrodite, where voids and impurity phases are seen from the processing/assembly steps in the *pristine cell*, as well as a large number of cracks from cycling in the *shorted cell*. Since failure in the cells occurs through filling of Li metal into cracks that span the entire SE thickness, differentiating cracks that are associated with a high stress concentration helps to highlight features that are more likely to cause cell failure. The combination of multimodal techniques as employed here is essential to differentiate such features, thus creating a hierarchy of degradation features based on the stress fields they create around them locally, in turn linking them to their propensity to contribute to cell failure.

However, caution needs to be exercised going forward toward *operando* studies, which will be even more valuable. For such experiments, the scanning time needs to be significantly reduced by reducing the cell size, while still mitigating the artifacts from cell assembly such as air leakage, which already seem to play a role. Categorizing cracks based on their associated stress fields can also be leveraged to reduce such *operando* studies to a manageable time-frame. Initial cell cycling can lead to numerous cracks, and following the morphological stress evolution of local regions of interest centered around regions of interest comprising of those that cause the highest local stresses can be used to conduct scans from beginning to end of life of such cells. Additionally, the deformation fields in this investigation represent the elastic strain, rather than the complete strain, which is a total of elastic and plastic components of strain. In brittle ceramic materials such as argyrodite, the plastic component of strain is small compared to the elastic component, and so such an approach is a fair approximation. However, in other systems where the ductility is greater, the total strain may be more appropriate.

Finally, the combination of X-ray imaging and scattering presented here will have relevance to other energy storage devices beyond the cells studied here. Every energy storage system undergoes degradation via some combination of diverse mechanisms. Additionally, the movement of ions between electrodes typically creates a change in the volume of the electrodes, which produces localized stress. As per the degradation mechanisms, this local stress can be due to chemical, mechanical, electrochemical, or even thermal degradation.[34] Application to cases ranging from high-Ni/Co-free cathodes,[50] to Si[51] or Sn-based[52] anodes, where volume expansion is a known problem, can be envisaged. In summary, using an approach with the objective of isolating degradation mechanisms, and directly tying them to their associated deformation fields effectively reduces a complex *electro-chemo-mechanical* problem into a stress minimization problem. This simplified problem statement then lends itself to the rational mitigation of degradation, and design of improved devices.

© 2024 The Author(s). Advanced Energy Materials published by Wiley-VCH GmbH

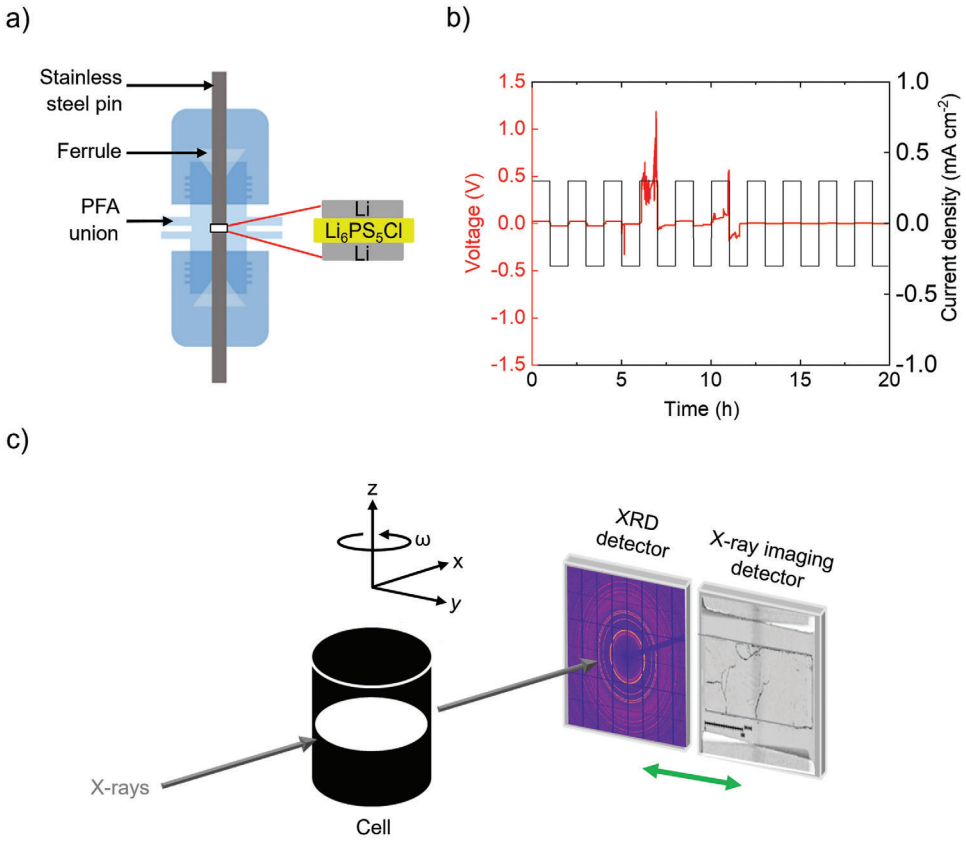


Figure 6. Experimental procedure. a) Schematic of the in situ cylindrical cell, and its components. For the cells prepared, Li_6PS_5Cl pellet was 3 mm dia. and Li foils were 2.5 mm dia. b) shows electrochemical cycling data for the *shorted cell*. Clear voltage spikes are visible, leading to shorting and failure of the cell after ≈12 h. c) Experimental layout for the in situ measurements. The cell was mounted on two translation and one rotation motor, while the downstream detectors were switchable between diffraction and imaging mode, for XRD-CT and μ-CT measurements respectively.

3. Conclusion

We report in situ, 3D, multimodal X-ray methods with the aim to gain a deeper understanding of degradation in Li|Li_6PS_5Cl|Li cells. Specifically, we show:

1) The degradation close to the interface is notably larger compared to the bulk of the solid-state electrolyte. The degradation is morphological, chemical, and electrochemical in nature.
2) The resultant deformation from this interfacial degradation is such that elevated stresses are produced, reaching an order of magnitude higher than the reported yield stress of Li.
3) Local stress hotspots are present throughout the volume of the SE, arising from various mechanisms. An interplay between SE processing, cell fabrication, and cycling are all seen to create significant stress concentrations around some features, while other cracks do not show an elevated strain around them, thus allowing differentiation of the ones which most influence cell lifetime.

Experimentally, this work underlines the importance of factors prior to cell cycling (such as cell assembly) in determining the SSB deformation. Furthermore, the 3D stress maps created are an important tool for the modeling community, to experimentally validate different degradation mechanisms, and how to model stress mitigation strategies in SSBs. Going forward, applying these new tools under *operando* conditions will require a careful optimization of the cell design, in terms of air exposure, size, SE chemistry, microstructure, and macroscopic stresses.

4. Experimental Section

Electrolyte Pellet Fabrication, Cell Assembly and Cycling: Lithium thiophosphate chloride solid electrolyte (Li_6PS_5Cl; 99.9%, Ampcera Inc.) pellets were produced using a 3 mm dia. stainless steel die (MSE Supplies). A uniaxial pressure of 280 MPa was applied using a hydraulic press (MTI, YLJ-15L) to compact about 6 mg of powder. After removal from the die, the pellets were wrapped in carbon paper (AvCarb P50, Fuel Cell Store) and placed in an alumina crucible (Almath) before a 15 min annealing step at 300 °C under vacuum in a Buchi oven to densify the electrolyte samples. The density of finished pellets was 1.58 gcm^{-3}, which is within 95 % of the reported density.[53] Lithium metal foils (Goodfellow, 0.1 mm thickness) were punched into 2.5 mm dia. discs before use. Subsequently, a Li|Li_6PS_5Cl|Li sandwich structure was assembled in a Swagelok cell, as shown in **Figure 6a**. Prior to assembly, the Swagelok cell components were dried overnight in a preheated drying chamber (binder ED 56) at 80°C. A cylindrical cell geometry and low density polymeric materials were chosen for optimal tomographic imaging and minimal interaction of the cell body with X-rays respectively. It was noted that the steel pins in the cell provide an easy mounting mechanism for rotation, as well as electrical contacts. The entire pellet fabrication, cell assembly process and cycling

© 2024 The Author(s). Advanced Energy Materials published by Wiley-VCH GmbH

was carried out in an Ar-filled glove box (MBraun, <1 ppm H_2O and O_2). A potentiostat (Reference 600+, Gamry) was used to conduct lithium plating/stripping for the *shorted cell* without additional stack pressure at room temperature. The cycling behavior of the *shorted cell* is shown in Figure 6b.

X-Ray Micro-Computed Tomography: Synchrotron-based X-ray micro-computed tomography (μ-CT) was carried out across two beamlines at ESRF (The European Synchrotron): ID15A[54] and ID19. For the *pristine cell*; a pink X-ray beam from a 17 pole undulator (peak energy at 26.5 keV) was used at the ID19 Beamline. A LuAG screen was used as scintillator to convert the X-ray absorption image into a visible light image. A CMOS detector (PCO-edge 5.5, 2560 × 2160) was coupled with a ×10 magnification optic to reach an effective pixel size of 0.65 μm. The detector was placed at a distance of 700 mm from the cell to optimize the phase contrast signal. For the *shorted cell*, a monochromatic X-ray beam with an energy of 72.5 keV was used at Beamline ID15A. A similar PCO-edge detector (2560 × 2160) with an effective pixel size of 0.70 μm was placed 300 mm away from the cell. Since the field of view was less than the diameter of the cell, the tomography scans were conducted with the center of the tomographic rotation at the edge of the recorded frame, to allow for an extended field of view, thus covering the entire cell diameter with a small pixel size.[55] For both cells, the tomwer (nabu) pipeline was used to apply a phase retrieval filter and compute the filtered back projections reconstructions.[56] Subsequently, Avizo 3D 2022.1 (Thermo Scientific) was used to perform threshold-based segmentation on the *pristine cell* and *shorted cell*. In this case, the cracks were segmented from the Li_6PS_5Cl volume. The reader is referred to the Section S1 (Supporting Information) for more detailed information on the reconstruction and segmentation parameters.

X-Ray Diffraction Computed Tomography: X-ray diffraction computed tomography (XRD-CT) was performed at beamline ID15A at ESRF. The setup at ID15A allows for holding the sample in place while swapping the (μ-CT) and XRD detectors within minutes, allowing for easier spatial correlation of 3D datasets from these techniques. A monochromatic, micro-focused X-ray beam was rastered horizontally and vertically across the volume of interest, while rotating the cell over 360° to collect XRD patterns at angular projections for every location of the cell. A DECTRIS Pilatus3 X CdTe 2M area detector was placed 1200 mm from the cell, and used to collect the diffractograms. For the *pristine cell*, KB mirrors were used to focus a 100 keV beam down to 5 μm (horizontal) × 2.5 μm (vertical) size. For the *shorted cell*, two-dimensionally focusing compound refractive lenses (CRLs) were used on a 72.5 keV monochromatic beam, to focus it down to 10 μm (horizontal) × 5 μm (vertical). The step size for rastering was equal to the size of the beam on the sample. It was noted that due to the high energy of X-rays, the transmission through both samples was > 95%. A Cr_2O_3 powder(NIST standard reference material 674b) was used for the detector geometrical corrections. Subsequently, pyFai[57] was used to azimuthally integrate the 2D diffractograms. Next, an in-house script was used to tomographically reconstruct the diffractograms into Cartesian space using a filtered back projection-based approach. Further details on the XRD-CT integration and reconstruction are included in Section S2.1 (Supporting Information). It was noted that the XRD-CT of the *pristine cell* was not carried out over the entire volume, as the μ-CT did not show significant degradation on the length scale of XRD-CT (≈10 μm). Thus, discreet sub-volumes at increasing distances from the Li|Li_6PS_5Cl interface were scanned, instead of continuously scanning the volume. The values used in Figure 3 for the *pristine cell* use the average of both sub-volumes to calculate the phase fraction/strain.

Rietveld Refinements: Sequential Rietveld refinements were performed at each voxel using TOPAS-7 for phase quantification, and strain estimation. Seven crystalline phases were fit in the XRD-CT dataset: i) Li_6PS_5Cl, ii) Li_2S, iii) LiCl, iv) Li_2CO_3, v) Li_2C_2, vi) graphite, and viii) Li_3P. This phase list contains the SE (Li_6PS_5Cl), the product after SE reduced by lithium (LiCl, Li_2S),[15,58] species from the heat treatment of the SE (graphite, Li_2C_2), and products from air exposure/cycling degradation (Li_3P, Li_2CO_3). A notable absence among these phases is metallic Li. A combination of a low atomic number (relatively low scattering, resulting in peaks with low intensity), as well as lack of a good powder pattern wherever there was metallic Li within the Li_6PS_5Cl made the reconstruction of Li challenging. Instead, the degradation due to metallic Li in the SE was tracked by monitoring other Li-containing species, such as LiCl and Li_2CO_3. A Pseudo-Voigt profile was used to fit the peaks from the various phases. After the refinement, the residuals were plotted against the refined parameters, to ensure no correlations. Further details on the Rietveld analysis are included in the Section S2.2 (Supporting Information).

Supporting Information

Supporting Information is available from the Wiley Online Library or from the author.

Acknowledgements

The authors acknowledge Beamlines ID15A and ID19 at The European Synchrotron (ESRF) for the experiments (IH-CH-1626, https://doi.esrf.fr/10.15151/ESRF-ES-856454454 ; MA-5422, https://doi.esrf.fr/10.15151/ESRF-ES-1030393436 ; IH-MI-1512, https://doi.esrf.fr/10.15151/ESRF-ES-1094854472). The authors gratefully acknowledge Dr. David N. Agyeman-Budu for the use of his beamtime (MA-5422) at ID15A, and Dr. Stefano Checchia for helping in setting up data analysis pipelines for Rietveld refinements. J.H., A.R., R.J. and P.R.S. acknowledge funding from the Faraday Institution through the LiSTAR program (FIRG058, EP/S003053/1) and degradation project (FIR0060, EP/003053/1). A.R. acknowledges the EPSRC for funding (EP/W029235/1) and UCL for start-up funds. R.S.Y. and R.J. also acknowledge funding from EPSRC and Horiba (EP/T517793/1). B.L., P.J.W. and P.P.P. are grateful for funding by EPSRC for the International Center to Center Collaboration with the ESRF grant reference EP/W003333/1 and the Henry Royce Institute established through EPSRC grants EP/R00661X/1, EP/P025498/1 and EP/P025021/1. P.R.S. was supported by the Department of Science, Innovation and Technology (DSIT) and the Royal Academy of Engineering under the Chair in Emerging Technologies program (CiET1718/59).

Conflict of Interest

The authors declare no conflict of interest.

Author Contributions

J.H. and R.Y.S. performed data analysis and manuscript writing, as well as cell construction and cycling. B.L. and L.B. assisted with data analysis and experiments on the imaging datasets. R.J., P.R.S., P.J.W., and A.R. acquired funding, assisted with data interpretation, and writing of the manuscript. J.H., M.D.M., and P.P.P. conceptualized and conducted the synchrotron experiments, and performed data analysis and interpretation.

Data Availability Statement

The data that support the findings of this study are available from the corresponding author upon reasonable request.

Keywords

degradation, interfaces, solid-state battery, strain/stress, X-rays

Received: September 15, 2024
Revised: November 16, 2024
Published online:

© 2024 The Author(s). Advanced Energy Materials published by Wiley-VCH GmbH

[1] M. J. Wang, E. Kazyak, N. P. Dasgupta, J. Sakamoto, *Joule* **2021**, *5*, 1371.
[2] D. H. Tan, Y. S. Meng, J. Jang, *Joule* **2022**, *6*, 1755.
[3] K. N. Wood, M. Noked, N. P. Dasgupta, *ACS Energy Lett.* **2017**, *2*, 664.
[4] J. Charbonnel, N. Darmet, C. Deilhes, L. Broche, M. Reytier, P.-X. Thivel, R. Vincent, *ACS Appl. Energy Mater.* **2022**, *5*, 10862.
[5] P. Vadhva, J. Hu, M. J. Johnson, R. Stocker, M. Braglia, D. J. Brett, A. J. Rettie, *ChemElectroChem* **2021**, *8*, 1930.
[6] J. Janek, W. G. Zeier, *Nat. Energy* **2023**, *8*, 230.
[7] X.-Q. Zhang, X.-B. Cheng, Q. Zhang, *Adv. Mater. Interfaces* **2018**, *5*, 1701097.
[8] P. P. Paul, B.-R. Chen, S. A. Langevin, E. J. Dufek, J. N. Weker, J. S. Ko, *Energy Storage Mater.* **2022**, *45*, 969.
[9] R. F. Ziesche, T. M. Heenan, P. Kumari, J. Williams, W. Li, M. E. Curd, T. L. Burnett, I. Robinson, D. J. Brett, M. J. Ehrhardt, P. D. Quinn, L. B. Mehdi, P. J. Withers, M. M. Britton, N. D. Browning, P. R. Shearing, *Adv. Energy Mater.* **2023**, *13*, 2300103.
[10] Y. Kato, S. Hori, T. Saito, K. Suzuki, M. Hirayama, A. Mitsui, M. Yonemura, H. Iba, R. Kanno, *Nat. Energy* **2016**, *1*, 1.
[11] Y. Li, S. Song, H. Kim, K. Nomoto, H. Kim, X. Sun, S. Hori, K. Suzuki, N. Matsui, M. Hirayama, T. Mizoguchi, T. Saito, T. Kamiyama, R. Kanno, *Science* **2023**, *381*, 50.
[12] B. Pang, Y. Gan, Y. Xia, H. Huang, X. He, W. Zhang, *Front. Chem.* **2022**, *10*, 837978.
[13] D. H. Tan, E. A. Wu, H. Nguyen, Z. Chen, M. A. Marple, J.-M. Doux, X. Wang, H. Yang, A. Banerjee, Y. S. Meng, *ACS Energy Lett.* **2019**, *4*, 2418.
[14] X. Bai, Y. Duan, W. Zhuang, R. Yang, J. Wang, *J. Mater. Chem. A* **2020**, *8*, 25663.
[15] D. H. S. Tan, E. A. Wu, H. Nguyen, Z. Chen, M. A. T. Marple, J.-M. Doux, X. Wang, H. Yang, A. Banerjee, Y. S. Meng, *ACS Energy Lett.* **2019**, *4*, 2418.
[16] P. P. Paul, E. J. McShane, A. M. Colclasure, N. Balsara, D. E. Brown, C. Cao, B.-R. Chen, P. R. Chinnam, Y. Cui, E. J. Dufek, D. P. Finegan, S. Gillard, W. Huang, Z. M. Konz, R. Kostecki, F. Liu, S. Lubner, R. Prasher, M. B. Preefer, J. Qian, M.-T. F. Rodrigues, M. Schnabel, S.-B. Son, V. Srinivasan, H.-G. Steinrück, T. R. Tanim, M. F. Toney, W. Tong, F. Usseglio-Viretta, *Adv. Energy Mater.* **2021**, *11*, 2100372.
[17] T. Foroozan, S. Sharifi-Asl, R. Shahbazian-Yassar, *J. Power Sources* **2020**, *461*, 228135.
[18] S. Hao, J. J. Bailey, F. Iacoviello, J. Bu, P. S. Grant, D. J. Brett, P. R. Shearing, *Adv. Funct. Mater.* **2021**, *31*, 2007564.
[19] J. Tippens, J. C. Miers, A. Afshar, J. A. Lewis, F. J. Q. Cortes, H. Qiao, T. S. Marchese, C. V. Di Leo, C. Saldana, M. T. McDowell, *ACS Energy Lett.* **2019**, *4*, 1475.
[20] E. Kazyak, R. Garcia-Mendez, W. S. LePage, A. Sharafi, A. L. Davis, A. J. Sanchez, K.-H. Chen, C. Haslam, J. Sakamoto, N. P. Dasgupta, *Matter* **2020**, *2*, 1025.
[21] W. Manalastas Jr, J. Rikarte, R. J. Chater, R. Brugge, A. Aguadero, L. Buannic, A. Llordés, F. Aguesse, J. Kilner, *J. Power Sources* **2019**, *412*, 287.
[22] J. A. Lewis, F. J. Q. Cortes, M. G. Boebinger, J. Tippens, T. S. Marchese, N. Kondekar, X. Liu, M. Chi, M. T. McDowell, *ACS Energy Lett.* **2019**, *4*, 591.
[23] T. Krauskopf, R. Dippel, H. Hartmann, K. Peppler, B. Mogwitz, F. H. Richter, W. G. Zeier, J. Janek, *Joule* **2019**, *3*, 2030.
[24] F. Sun, C. Wang, M. Osenberg, K. Dong, S. Zhang, C. Yang, Y. Wang, A. Hilger, J. Zhang, S. Dong, H. Markötter, I. Manke, G. Cui, *Adv. Energy Mater.* **2022**, *12*, 2103714.
[25] S. Narayanan, U. Ulissi, J. S. Gibson, Y. A. Chart, R. S. Weatherup, M. Pasta, *Nat. Commun.* **2022**, *13*, 7237.
[26] Y. Zheng, S. Zhang, J. Ma, F. Sun, M. Osenberg, A. Hilger, H. Markötter, F. Wilde, I. Manke, Z. Hu, G. Cui, *Sci. Bull.* **2023**, *68*, 813.
[27] L. Porz, T. Swamy, B. W. Sheldon, D. Rettenwander, T. Frömling, H. L. Thaman, S. Berendts, R. Uecker, W. C. Carter, Y.-M. Chiang, *Adv. Energy Mater.* **2017**, *7*, 1701003.
[28] J. Duan, T. Fuchs, B. Mogwitz, P. Minnmann, T.-T. Zuo, A. Henss, J. Janek, *Mater. Today* **2023**, *70*, 33.
[29] S. Hao, S. R. Daemi, T. M. Heenan, W. Du, C. Tan, M. Storm, C. Rau, D. J. Brett, P. R. Shearing, *Nano Energy* **2021**, *82*, 105744.
[30] J. Kasemchainan, S. Zekoll, D. Spencer Jolly, Z. Ning, G. O. Hartley, J. Marrow, P. G. Bruce, *Nat. Mater.* **2019**, *18*, 1105.
[31] Z. Ning, G. Li, D. L. R. Melvin, Y. Chen, J. Bu, D. Spencer-Jolly, J. Liu, B. Hu, X. Gao, J. Perera, C. Gong, S. D. Pu, S. Zhang, B. Liu, G. O. Hartley, A. J. Bodey, R. I. Todd, P. S. Grant, D. E. J. Armstrong, T. J. Marrow, C. W. Monroe, P. G. Bruce, *Nature* **2023**, *618*, 287.
[32] Z. Ning, D. S. Jolly, G. Li, R. De Meyere, S. D. Pu, Y. Chen, J. Kasemchainan, J. Ihli, C. Gong, B. Liu, D. L. R. Melvin, A. Bonnin, O. Magdysyuk, P. Adamson, G. O. Hartley, C. W. Monroe, T. J. Marrow, P. G. Bruce, *Nat. Mater.* **2021**, *20*, 1121.
[33] D. P. Finegan, A. Vamvakeros, C. Tan, T. M. Heenan, S. R. Daemi, N. Seitzman, M. Di Michiel, S. Jacques, A. M. Beale, D. J. Brett, P. R. Shearing, K. Smith, *Nat. Commun.* **2020**, *11*, 631.
[34] T. M. M. Heenan, I. Mombrini, A. Llewellyn, S. Checchia, C. Tan, M. J. Johnson, A. Jnawali, G. Garbarino, R. Jervis, D. J. L. Brett, M. Di Michiel, P. R. Shearing, *Nat. (London)* **2023**, *617*, 507.
[35] H. Liu, S. Kazemiabnavi, A. Grenier, G. Vaughan, M. Di Michiel, B. J. Polzin, K. Thornton, K. W. Chapman, P. J. Chupas, *ACS Appl. Mater. Interfaces* **2019**, *11*, 18386.
[36] K. M. Jensen, X. Yang, J. V. Laveda, W. G. Zeier, K. A. See, M. Di Michiel, B. C. Melot, S. A. Corr, S. J. Billinge, *J. Electrochem. Soc.* **2015**, *162*, A1310.
[37] J. Sottmann, M. Di Michiel, H. Fjellvåg, L. Malavasi, S. Margadonna, P. Vajeeston, G. B. Vaughan, D. S. Wragg, *Angew. Chem., Int. Ed.* **2017**, *56*, 11385.
[38] X. Randrema, C. Barcha, M. Chakir, V. Viallet, M. Morcrette, *Solid State Sci.* **2021**, *118*, 106681.
[39] L. Zhou, K.-H. Park, X. Sun, F. Lalère, T. Adermann, P. Hartmann, L. F. Nazar, *ACS Energy Lett.* **2018**, *4*, 265.
[40] S. Shishvan, N. Fleck, R. McMeeking, V. Deshpande, *Electrochimica acta* **2023**, *467*, 143081.
[41] Z. Deng, Z. Wang, I.-H. Chu, J. Luo, S. P. Ong, *J. Electrochem. Soc.* **2016**, *163*, A67.
[42] J. Aspinall, D. E. Armstrong, M. Pasta, *Mater. Today Energy* **2022**, *30*, 101183.
[43] C. Xu, Z. Ahmad, A. Aryanfar, V. Viswanathan, J. R. Greer, *Proc. Natl. Acad. Sci.* **2017**, *114*, 57.
[44] W. S. LePage, Y. Chen, E. Kazyak, K.-H. Chen, A. J. Sanchez, A. Poli, E. M. Arruda, M. Thouless, N. P. Dasgupta, *J. Electrochem. Soc.* **2019**, *166*, A89.
[45] D. K. Singh, A. Henss, B. Mogwitz, A. Gautam, J. Horn, T. Krauskopf, S. Burkhardt, J. Sann, F. H. Richter, J. Janek, *Cell Rep. Phys. Sci.* **2022**, *3*, 101043.
[46] C. Lee, S. Y. Han, J. A. Lewis, P. P. Shetty, D. Yeh, Y. Liu, E. Klein, H.-W. Lee, M. T. McDowell, *ACS Energy Lett.* **2021**, *6*, 3261.
[47] C. D. Fincher, C. E. Athanasiou, C. Gilgenbach, M. Wang, B. W. Sheldon, W. C. Carter, Y.-M. Chiang, *Joule* **2022**, *6*, 2794.
[48] Y. Xiao, Y. Wang, S.-H. Bo, J. C. Kim, L. J. Miara, G. Ceder, *Nat. Rev. Mater.* **2020**, *5*, 105.
[49] S. Shishvan, N. Fleck, R. McMeeking, V. Deshpande, *Eur. J. Mech., A, Solids* **2023**, *100*, 104998.
[50] S. Schweidler, L. de Biasi, G. Garcia, A. Mazilkin, P. Hartmann, T. Brezesinski, J. Janek, *ACS Appl. Energy Mater.* **2019**, *2*, 7375.
[51] L. Sun, Y. Liu, R. Shao, J. Wu, R. Jiang, Z. Jin, *Energy Storage Mater.* **2022**, *46*, 482.

© 2024 The Author(s). Advanced Energy Materials published by Wiley-VCH GmbH

[52] S.-C. Chao, Y.-F. Song, C.-C. Wang, H.-S. Sheu, H.-C. Wu, N.-L. Wu, *J. Phys. Chem. C* **2011**, *115*, 22040.
[53] L. Zhou, K.-H. Park, X. Sun, F. Lalère, T. Adermann, P. Hartmann, L. F. Nazar, *ACS Energy Lett.* **2018**, *4*, 265.
[54] G. B. M. Vaughan, R. Baker, R. Barret, J. Bonnefoy, T. Buslaps, S. Checchia, D. Duran, F. Fihman, P. Got, J. Kieffer, S. A. J. Kimber, K. Martel, C. Morawe, D. Mottin, E. Papillon, S. Petitdemange, A. Vamvakeros, J.-P. Vieux, M. Di Michiel, *J. Synchrotron Radiat.* **2020**, *27*, 515.
[55] A. Kyrieleis, M. Ibison, V. Titarenko, P. J. Withers, *Nucl. Instrum. Methods Phys. Res. Sect. A. Accel. Spectrom. Detect. Assoc. Equip.* **2009**, *607*, 677.
[56] P. Paleo, H. Payno, N. Vigano, C. Nemoz, Nabu 2021.2.0, **2022**.
[57] J. Kieffer, D. Karkoulis, in *Journal of Physics: Conference Series*, vol. *425*, IOP Publishing, Bristol, England **2013**, p. 202012.
[58] Y. Zhou, C. Doerrer, J. Kasemchainan, P. G. Bruce, M. Pasta, L. J. Hardwick, *Batter. Supercaps* **2020**, *3*, 647.

© 2024 The Author(s). Advanced Energy Materials published by Wiley-VCH GmbH